ACS APPLIED NANO MATERIALS

www.acsanm.org Article

Fluence-Dependent Morphological Transitions in Laser-Induced Graphene Electrodes on Polyimide Substrates for Flexible Devices

Moataz Abdulhafez, Golnaz N. Tomaraei, and Mostafa Bedewy*

Cite This: ACS Appl. Nano Mater. 2021, 4, 2973−2986 Read Online

ACCESS | Metrics & More | Article Recommendations | Supporting Information

ABSTRACT: Laser carbonization of polymers is an emerging technique that enables directly patterning conductive carbon electrodes for a plethora of flexible devices, including supercapacitors and sensors. While these laser-induced nanocarbon (LINC) patterns were previously shown to have various hierarchical porous and fibrous graphene-based morphologies, the fundamental mechanisms underlying the formation of specific LINC morphologies is still largely missing. Here, we present a method for lasing polyimide films with spatially controlled gradients of optical energy flux. Combined with Gaussian beam modeling, our approach uniquely enables continuously sweeping different laser fluence values as a spatial map along the laser path. We find that above the fluence value of 5 J/cm^2, progressive carbonization and swelling results in porous LINC. We also identify two additional thresholds that correspond to morphological transitions: first, from isotropic porous morphology to anisotropic networks at 12 J/cm^2; second, from anisotropic networks to aligned nanofibers at 17 J/cm^2. Our results show that anisotropic cellular networks are the most electrically conducting and have the highest quality sp^2 carbon. However, the aligned woolly nanofiber morphology is electrically insulating along the length of the lased lines, although they exhibit the highest degree of carbonization with the least heteroatom content. Hence, our results provide insights into the fluence-dependence of the physicochemical processes underlying LINC formation. Moreover, our approach enables generating a morphology diagram for LINC, which facilitates precise tunability of both the morphology and properties of LINC patterns, based on easy-to-control processing parameters, such as laser power and degree of beam defocusing.

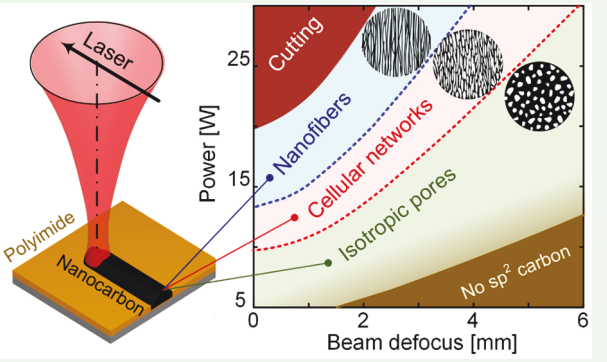

KEYWORDS: *direct laser writing, laser-induced graphene, carbon nanofibers, conducting electrodes, flexible electronics*

INTRODUCTION

The use of lasers to locally carbonize commercial polymers, such as polyimide, is an emerging technique for the fabrication of functional graphenic nanocarbons directly on flexible substrates.[1−6] This direct-write approach is a powerful alternative to printing technologies, which use nanocarbon-containing inks to print conducting electrodes of carbon nanotubes or graphene in flexible device fabrication.[7,8] In fact, before the recent interest in flexible electronics, laser processing of polymers (especially polyimide) was first studied in the context of polymer ablation using UV pulsed lasers.[9] However, in addition to the dissociation of its polymeric structure, carbonization and enhanced conductivity were observed using both pulsed[10−13] and continuous wave (CW)[14,15] UV lasers, as well as pulsed[13,16,17] and CW visible light[18,19] lasers. Accordingly, micron-scale conductive electrodes were fabricated on polyimide for electrochemical and electronic devices.[11,14] More recently, it was reported that rastering a CW CO_2 laser in air creates patterns of porous graphene-based structures on polyimide.[1] Importantly, these conductive patterns were used to develop a plethora of devices including micro supercapacitors,[2] strain or piezoresistive sensors,[20,21] multifunctional strain sensors,[22] pH sensors,[20] gas sensors,[23] flexible electrodes,[24] antifouling surfaces,[25] wearable sensors,[26] artificial throat,[27] microfluidic devices,[28] and heating elements.[29] Owing to the diversity of morphologies achievable by laser carbonization, here we use the term laser-induced nanocarbon (LINC), as a more general term than laser-induced graphene to collectively refer to all nanostructured carbon materials fabricated by laser irradiation of polymer precursors.

A key challenge is to understand the process−structure−property relationships for LINC formation. Importantly, how does laser condition (wavelength, power, speed, pulse rate, etc.) affect the resulting LINC morphology? In turn, how does

Received: January 13, 2021
Accepted: March 3, 2021
Published: March 11, 2021

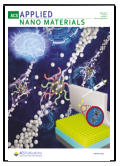

https://dx.doi.org/10.1021/acsanm.1c00101
ACS Appl. Nano Mater. 2021, 4, 2973−2986

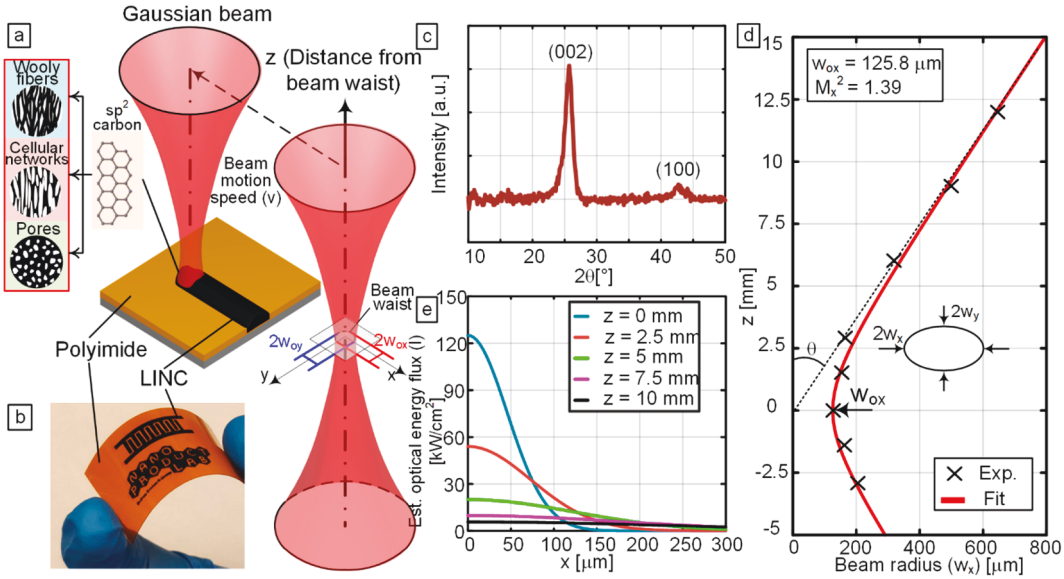

Figure 1. (a) Schematic of lasing flat untilted polyimide to produce a LINC line with a Gaussian beam, illustrating the transformation of polyimide to sp^2 carbon and the type of morphologies resulting in the process. (b) Photograph of a 2D LINC pattern on a flexible polyimide substrate. (c) XRD of powdered LINC lased at P = 28 W, v = 500 mm/s, z = 0 mm. (d) Experimental points representing the estimated laser beam profile along the lasing direction x using the knife edge technique, along with the profile of the fitted Gaussian beam illustrating the divergence of the beam away from the beam waist. The resulting beam spot in the x direction is estimated to be $2w_{ox}$ = 251.6 μm. (e) Estimated optical flux along the x direction at constant power (P = 22.5 W), showing the change of beam intensity with z (i.e., with changing spot size by defocusing the beam).

the morphology and chemical composition of LINCs affect their properties such as electrical conductivity and electrochemical behavior? While the morphology of LINC is generally described in literature as porous, there are reports indicating that LINC's morphological structure can be tuned with varying laser parameters.[30,31] In particular, it was observed that increasing laser-induced thermal damage can result in fibrous[32] or porous formations[14] in pulsed laser irradiation of polyimides. Using CO_2 lasers, Lamberti et al. reported that by varying the scan speed of the laser and the pulse width modulation (PWM) frequency, different morphologies of LINC were observed that were described as "sheets", "needles" and "porous" morphologies.[31] However, the precise mapping of laser conditions that lead to these differences in terms of universally recognizable physical quantities such as laser fluence is still largely missing. Moreover, identifying the transition thresholds between these morphologies has been challenging, because previous work has relied on discrete experiments exploring the large parameter space,[33] owing to the lack of facile approaches that can enable applying continuous gradients of laser parameters on the same sample.

Duy et al.[30] recently reported that by changing the laser parameters (area rastering parameters and PWM duty cycle) carbon nanofibers were produced, which was attributed to low pixel density in laser rastering. This is explained by the fact that high laser density leads to increased overlap between the laser paths, which would lead to the destruction of any fibers forming in the process. This approach of varying the pixel density in two-dimensional rastering was also recently used to tune surface hydrophobicity over large areas.[28] However, for applications of LINC that require high resolution patterning,[2,6] wherein only micron-scale nonoverlapping lines are lased on the surface, we need to investigate the independent effects of spatiotemporal optical energy flux on the formation of different types of sp^2-hybridized nanocarbons in a single lasing process. Hence, this inherent process-structure−property relation of LINC formation needs to be decoupled from the proximity effects that govern collective properties over large areas.

In this study, we leverage laser fluence gradients and beam defocus to facilitate understanding LINC formation process by quantitatively correlating laser condition, the resulting LINC morphologies, and their varying electrical conductivity. Additionally, we describe methods of creating LINC materials with spatially varying morphologies and hence spatially varying properties. In particular, to investigate the effect of tuning fluence on morphology and properties, we uniquely combine mathematical modeling of Gaussian laser beams with two experimental approaches to control the local spread of the beam: (1) lasing individual lines on a tilted polyimide surface to achieve controlled gradients of fluence, and (2) lasing untilted samples at different degrees of defocusing for spatially uniform LINC lines. The first approach enable studying the evolution of nanoscale morphology and atomic structure continuously at different fluence values on the same polyimide film. Thus, we can precisely identify fluence thresholds for transition between different LINC morphologies owing to the resulting spatial map of fluence along a single LINC line in the tilted experiments. On the basis of our findings, we propose a model for the morphological evolution during laser carbonization that results in nanoporous structures, cellular networks, and woolly fibers at different fluence values, which enables delineating a clear morphology diagram. We also correlate these results with electrical conductivity measurements to reveal the process-structure−property relationships governing the design of LINC materials with tunable and spatially varying properties.

RESULTS AND DISCUSSION

Tunable Beam Intensity for Patterning Graphitic LINC on polyimide. LINCs form due to the local interaction of a laser beam with the surface of polyimide. As shown

https://dx.doi.org/10.1021/acsanm.1c00101
ACS Appl. Nano Mater. 2021, 4, 2973−2986

schematically in Figure 1(a), a continuous beam with power P is scanned across the polyimide film at a speed v with the sample surface at a distance z from the beam waist. Photothermal interactions from the radiation absorption by the polyimide drive a rapid temperature increase that carbonizes polyimide locally at the moving laser spot to create a pattern, as depicted in Figure 1(b). Depending on the lasing parameters, the polyimide can be carbonized into nanoscale graphene-rich domains, as shown from X-ray diffraction (XRD) results in Figure 1(c). These results were generated for individual LINC lines, which are formed at power P = 28 W, speed v = 500 mm/s, and distance from beam waist z = 0 mm. From XRD, we can clearly identify the (002) and (100) peaks that are characteristic of highly ordered sp^2-hybridized graphitic carbon.

The laser beam profile of the CW CO_2 laser used in this study is depicted in Figure 1(d), estimated from beam characterization experiments (see Methods Section). CW CO_2 lasers are used for LINC applications primarily because polyimide has high absorptance for the infrared (IR) range around the wavelength of CO_2 laser (λ = 10.6 μm),[34] and hence it carbonizes relatively easily. Since more than 90% of IR at this wavelength is absorbed by the top surface of polyimide,[34] the properties of the underlying surface beneath the polyimide film does not affect LINC formation. Moreover, CO_2 laser systems are commercially available at low cost, which paves the way for widespread adoption of this approach for fabrication of functional electrodes on flexible devices. Beam power and profile measurements are used to estimate the laser intensity profile at the different z values at different spot sizes and powers. An example is shown in Figure 1(e) which shows the change of intensity across the beam for different z values at the same laser power. At different z values, the beam intensity $I(x,y)$ follows a Gaussian distribution with the narrowest distribution featuring the overall maximum value of intensity at the beam waist where z = 0 mm. Changing both the speed and the spot size changes the dwell time of the laser spot,[35] which corresponds to how long a point is exposed to the moving laser beam. Naturally, faster speeds reduce the dwell time. At a fixed speed, however, the dwell time also decreases with decreasing spot size as shown in the Figure S1(a) of the Supporting Information, SI. The relationship between the beam dwell time and the laser intensity controls the value of the average fluence (estimated using the Gaussian beam model), which would in turn influence the temperature increase at a point as discussed in the Methods section. The change in average fluence delivered at different degrees of beam defocusing (i.e., different z values) and powers is shown in Figure S1(b).

Fluence Gradients for Spatial Control of LINC Morphology. To investigate the influence of beam intensity and fluence on polyimide carbonization, we create a gradient of fluence by lasing a tilted sample of polyimide. This tilt angle controls how different points on the substrate along the laser path experience different fluence levels. A schematic of the experiment is shown in Figure 2(a), where the sample is lased at an angle (γ = 45°). While the laser beam moves in a horizontal direction x at a speed v, the sample is tilted along the x' direction with angle γ between x and x'. Since the spot size changes with z, the beam maximum intensity, average fluence and dwell time also change along the x' direction (i.e., along the lased lines in the sample's plane). Tilting the axis normal to the sample (Z') with respect to the beam axis (Z) by

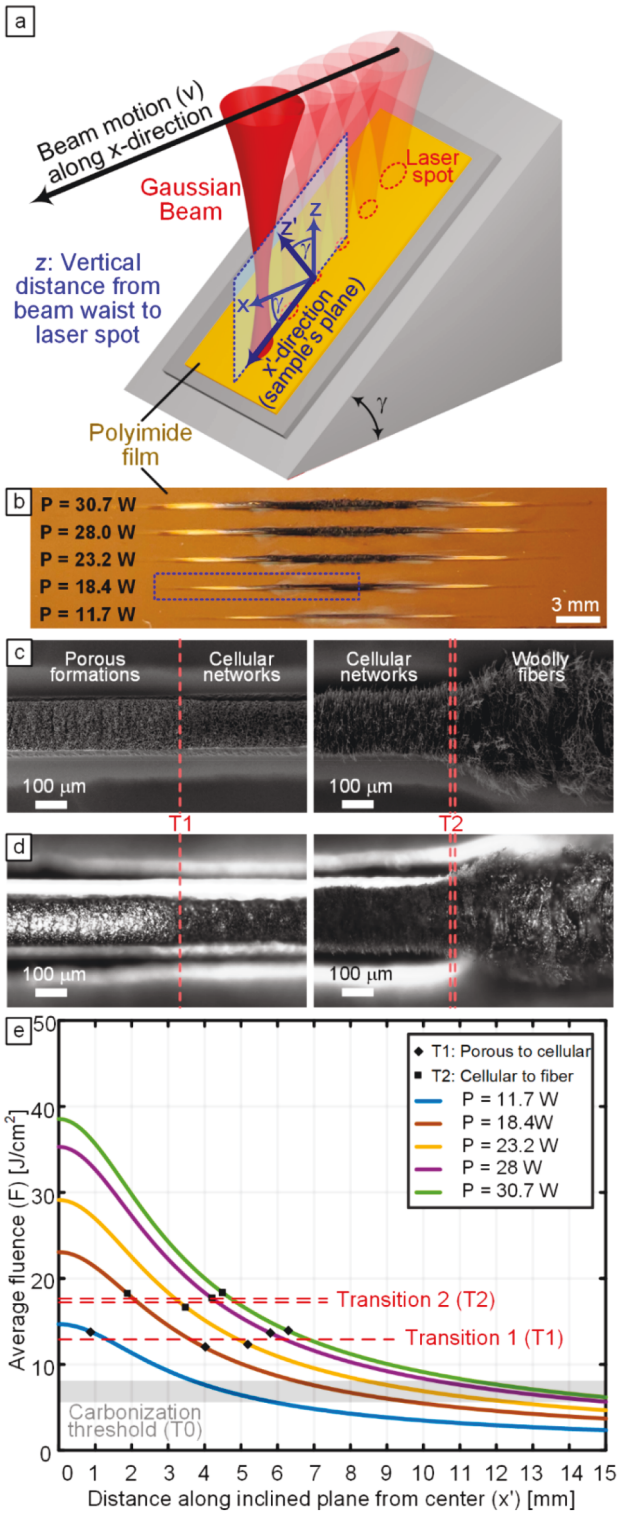

Figure 2. (a) Schematic of setup for LINC formed with gradient fluence by lasing tilted polyimide at an angle γ. The lines are lased along the x' in the sample's plane, while the beam moves along the x direction with speed v. (b) Optical photograph of the different lines lased at different powers using the method described in (a) at γ = 45°, showing the different color changes along the lased lines and the change of the location of the transition of LINC morphology as a function of powers. (c) SEM image of the two transitions from porous to cellular networks (T1) and from cellular networks to woolly fibers (T2) lased at power P = 18.4 W. (d) Optical microscopy images at the same points showing the change in line reflectivity for both

https://dx.doi.org/10.1021/acsanm.1c00101
ACS Appl. Nano Mater. 2021, 4, 2973−2986

Figure 2. continued

transitions and abrupt formation of woolly fibers. (e) Plot of estimated fluence delivered at different powers and v = 500 mm/s vs the distance from LINC line center in the x' direction. Locations of transitions T1 and T2 are marked with black diamond and square markers on the curves, respectively, showing that the transitions occur at similar fluence values around F_{T1} = 12 J/cm^2 and F_{T2} = 17 J/cm^2 (horizontal red lines of constant fluence). Horizontal gray band 5−8 J/cm^2 represents the estimated carbonization threshold.

γ changes the distribution of beam intensity and transforms the geometry of the beam spot as illustrated in Figure S2. In the SI, we demonstrate that the average fluence value for the untilted case is approximately equal to the tilted case for our values of beam parameters. This can be explained by the fact that the tilt angle does not drastically change the laser beam intensity profile, and that while the beam broadens, so does the beam spot. Hence, averaging over the area does not affect the averaged intensity over the spot when comparing the untilted to the tilted case.

The sample is lased at different powers ranging from P = 11.7 W to P = 30.7 W at a constant beam scanning velocity v = 500 mm/s with the resulting lased lines shown in Figure 2(b). Since, each point on the line represents a different average fluence value, the lines with gradient fluence uniquely enables mapping the fluence-dependent morphological evolution. Close to the edges of the visible lines, swelling of the polyimide is observed. Toward the center of the lines, carbonization is visible, and in some cases the formation of fuzzy/woolly fibers at the center was observed where fluence is highest. The length of the carbonized portion of the line where LINC is formed (black portion) increases with increasing P, which can be explained by shifts in the location, at which the threshold fluence for carbonization (estimated to be in the range of 5−8 J/cm^2) is reached, referred to here as transition T0.

More discrete transitions of LINC morphology along the lines are identified under both optical microscopy and scanning electron microscopy (SEM) imaging, as shown in Figure 2(c,d). The first type of transition (T1) observed is from a porous morphology to a cellular network morphology,

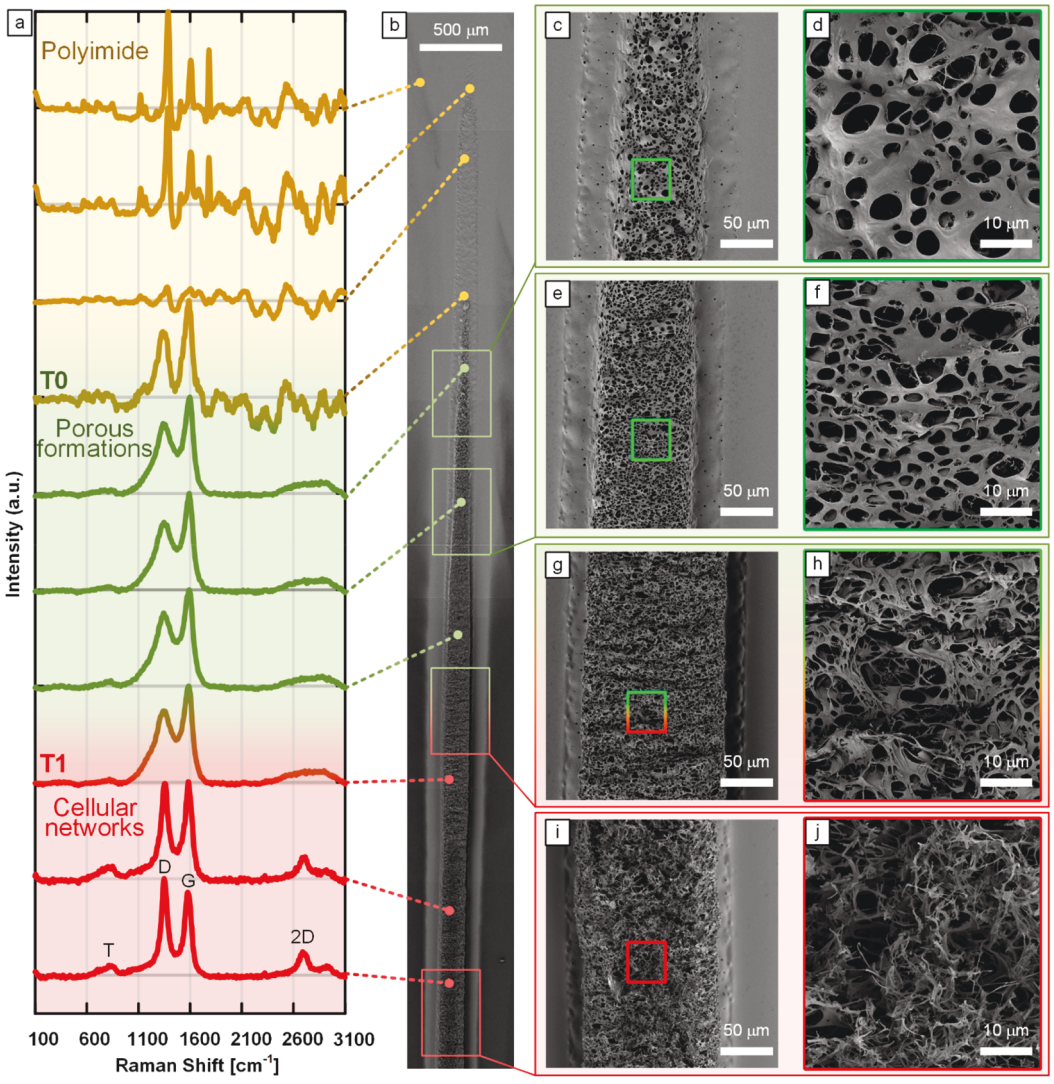

Figure 3. (a) Raman spectra of different points along the LINC line generated from tilted lasing at γ = 45°, power P = 11.7 W, and speed v = 500 mm/s, showing the carbonization transition from polyimide to porous LINC (T0) as well the transition from isotropic porous LINC to cellular networks (T1). (b) Stitched SEM images of lased line. (c−j) SEM images along the line illustrating the different morphologies.

https://dx.doi.org/10.1021/acsanm.1c00101
ACS Appl. Nano Mater. 2021, 4, 2973−2986

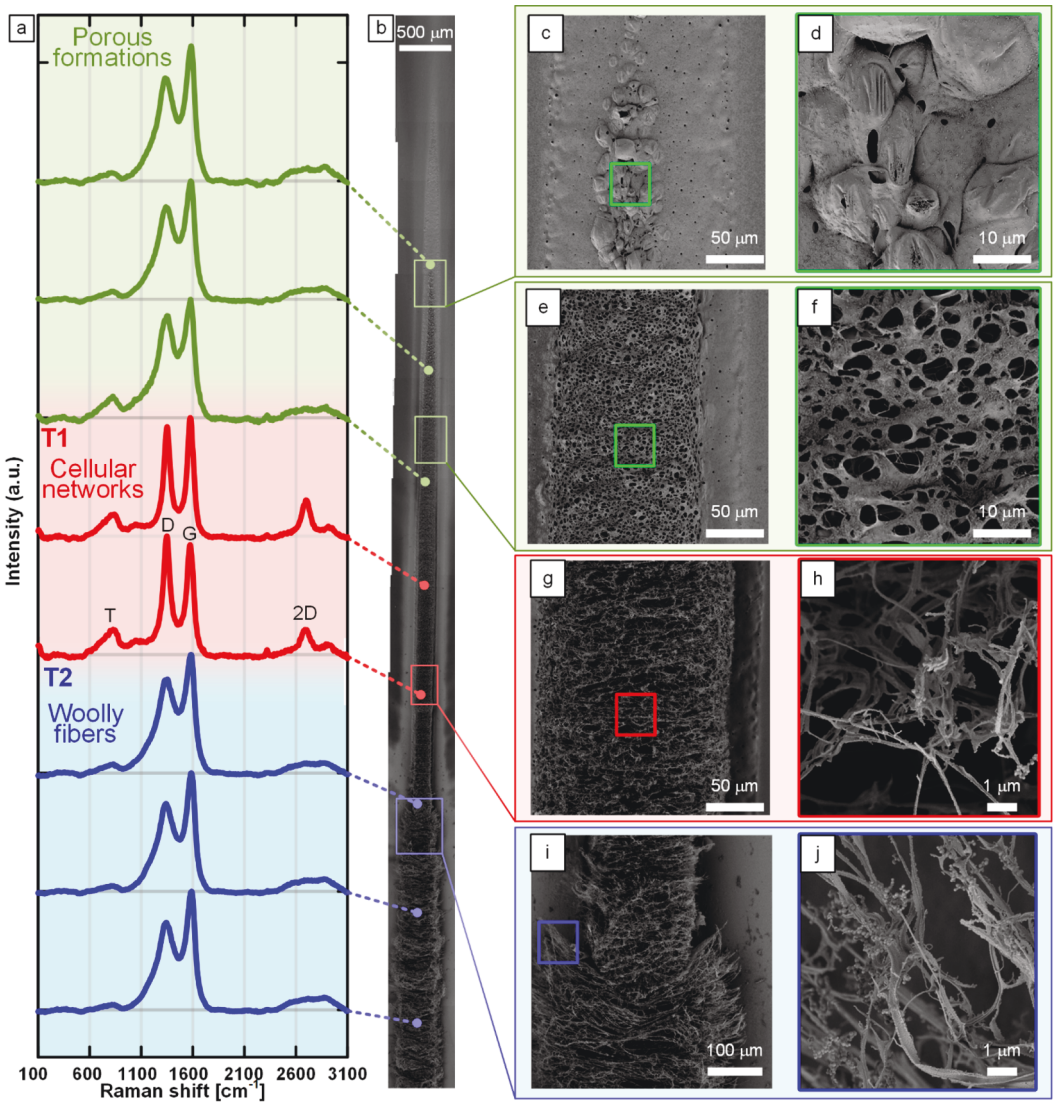

Figure 4. (a) Raman spectra of different points along the LINC line generated from tilted lasing at $\gamma = 45°$, power $P = 18.4$ W, and speed $v = 500$ mm/s, showing the transition from isotropic porous LINC to cellular networks (T1), as well as the transition to woolly fibers (T2). (b) Stitched SEM images of lased line. (c–j) SEM images along the line illustrating the different morphologies.

which is accompanied by a stark change in reflectivity as noticed in the optical images Figure 2(d). The second type of transition (T2) observed is an abrupt transition from the cellular networks to a large volume woolly fibrous formation. This second transition was only observed at powers larger than $P = 18.4$ W. The distance between the midpoint of the lines and the points of transition along the x' direction are plotted in Figure 2(e). The transitions (T1 and T2) are mapped with the average fluence estimated at the different powers and x' values according to our beam model presented in the Methods section. The plot indicates that the transitions occur at fixed average fluence values, which is a useful insight that we will build on later for creating a morphology diagram. The porous formation to cellular formation transition (T1 in Figure 2(e)) occurs at an estimated average fluence value of ~12 J/cm^2. The transition from cellular network to woolly fiber formations occurs at an estimated average fluence value of ~17 J/cm^2. It is also observed that while there is a porous to cellular network transition (T1) when the lasing power was $P = 11.7$ W, there is no network to fibers transition (T2) at this low power. This indicates that the fluence threshold for woolly fiber formation is higher than peak fluence in the center of the line at this power, which highlights the utility of our fluence-based mapping approach and our beam modeling. In addition to the fluence driven transitions, the resulting woolly fibers at the point of highest fluence (center of the lines) become more voluminous and wider with increasing power, as shown in Figure S3.

Structural Changes Concomitant with LINC Morphology Evolution. To correlate the observed morphologies from the tilted lasing experiment to the molecular structure of LINC, Raman spectroscopy mapping was carried out along the lased lines for two power values, $P = 11.7$ W (does not have woolly fibers at the center of the line) and $P = 18.4$ W (has woolly fibers at the center of the line), as shown in Figures 3 and 4. Raman spectra for different points along the lased line are shown in Figures 3(a) and 4(a), and top view SEM images of the lines are shown in Figures 3(b–j) and 4(b–j). For a comprehensive understanding of the evolution along the centimeters-long line, we stitched SEM images going from

https://dx.doi.org/10.1021/acsanm.1c00101
ACS Appl. Nano Mater. 2021, 4, 2973–2986

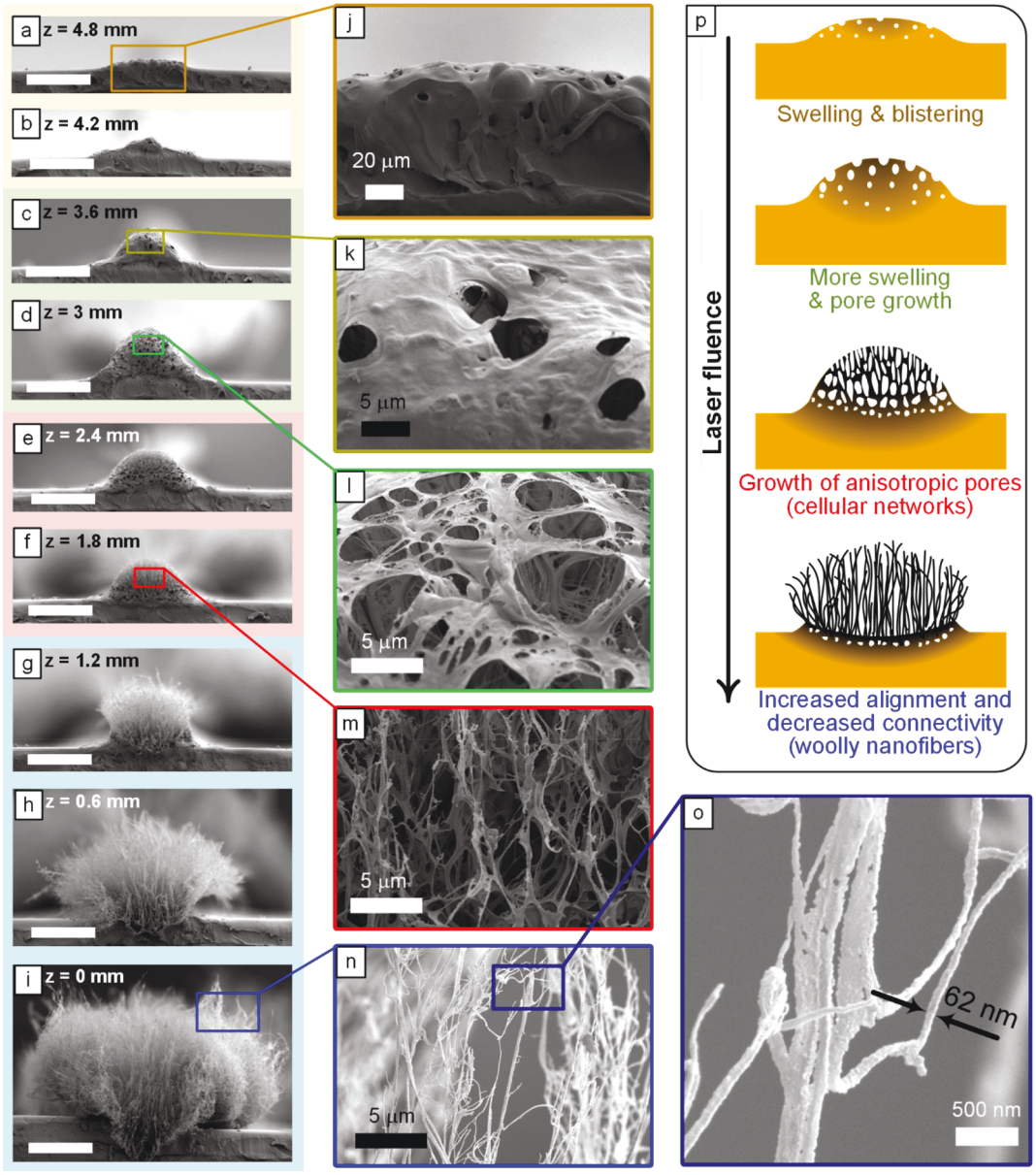

Figure 5. (a–i) SEM images of side views of the edge of polyimide films lased to generate LINC, while untilted ($\gamma = 0°$) at different z values (Scale bar: 100 μm). (j–o) Higher resolution SEM images. (j) SEM showing the swelling of polyimide. (k) SEM showing pore formation and growth. (i) SEM showing increase in pore shape anisotropy. (m) SEM showing the formation of anisotropic cellular networks. (n) SEM showing the formation of LINC nanofibers. (o) High resolution image showing ~60 nm nanofibers. (p) Schematic illustrating the evolution of LINC formation with increasing fluence, showing the transitions between different LINC morphologies.

the edge of the line to its center in Figures 3(b) and 4(b). Also, we present higher resolution SEMs of selected points along the line in Figures 3(c–j) and 4(c–j).

The Raman spectra at points toward the edge of the lines prior to the formation of porous LINC display the characteristic peaks of polyimide at a Raman shift of 1395,1601, and 1786 cm^{-1} associated with C–N–C axial vibration, imide ring vibration and C=O asymmetric ring, respectively. (The background signal due to polyimide fluorescence is removed).[16] Moving along the line with increasing average fluence, the Raman peaks associated with polyimide disappear and the G and D bands characteristic of graphenic nanocarbon appear, indicating the progression of carbonization after T0. The observed spectra exhibit G and D peaks with large full width at half-maximum (fwhm) and broadband band around the 2D peak. The spectra have the same shape along the lased line until a stark change in shape is observed beyond the T1 transition. In particular, a sharper well-defined 2D band appears, accompanied by a marked decrease in G and D peak fwhm (from 150 cm^{-1} to around 75 cm^{-1} for the G peak), as shown in Figures 3(a) and S4(a). The decrease of fwhm of the G peak indicates larger sp^2 grains.[36] Hence, these changes suggest the formation of well-defined graphene domains concomitant with the transition from isotropic porous morphology to more anisotropic (as will be shown later in Figure 5 from side-view SEMs) cellular networks of 3D graphene, as shown in the difference between Figure 3(f,j). A small peak is observed in the Raman spectra at 850 cm^{-1}, which was reported previously for laser carbonization of polyimide with a UV laser.[14] This peak is consistent with the T

https://dx.doi.org/10.1021/acsanm.1c00101
ACS Appl. Nano Mater. 2021, 4, 2973–2986

band representing sp^3 vibration density of states,[37,38] which was previously shown in ab initio calculations of Raman spectra.[39]

Similar analysis is performed for the lased line at P = 18.4 W (Figure 4), showing the same transitions take place at higher power. In this case, however, three morphologies are observed with both transitions T1 and T2 identifiable in Raman measurements and SEMs. At the T2 threshold, an abrupt transition into woolly fibrous morphology is observed [Figure 4(i,j)], which was not seen in the low-power (P = 11.7 W) results shown in Figure 3. Interestingly, the voluminous woolly fibers exhibit similar Raman spectra to the isotropic porous LINC that form between T0 and T1, with no sharp 2D peak and larger fwhm for the G peak (Figure S4 (b)) compared to the anisotropic cellular networks that form between T1 and T2. These results suggest that the fibrous LINC formed beyond T2 generally has lower-quality sp^2 carbon than the anisotropic cellular networked structure formed between T1 and T2. This is crucial for tailoring the properties of LINC patterns, as will be shown for electrical conductivity measurements below.

Fluence-Dependent Tunability of LINC Morphology. To gain more insight into the obtained LINC morphologies, untilted polyimide films are lased at different z values for the same power P = 18.4 W to change the average fluence values. SEM images of the side view of the films along the direction of lasing are shown in Figure 5(a−i), with high-resolution images shown in Figures 5(j−o). The images at the different levels of defocusing elaborate the evolution of the morphology with increasing average fluence (largest at z = 0 mm). At z = 4.8 mm, some swelling is observed in the morphology as shown in Figure 5(a,j). With more beam focusing (i.e., less defocusing with smaller z = 3.6 mm), more swelling of polyimide is observed along with the emergence of a clearly defined porous structure, having isotropic pores on the surface as shown in Figure 5(c,k). At z = 3 mm, the pores appear to be larger in size and more anisotropic, as shown in Figure 5(d,l). With further beam focusing, alignment emerges in a highly anisotropic cellular network structure at z = 1.8 mm, as shown in Figure 5(f,m). Approaching z = 0 mm, nanofibers form starting at z = 1.2 mm, with progressively more voluminous woolly morphology, as seen in Figure 5(i,n). High-resolution SEM imaging shows that nanofibers of ∼60 nm form at z = 0 mm Figure 5(o).

These transitions capture the evolution of LINC morphology with increasing average fluence values. A model of these fluence-dependent transitions is illustrated schematically in Figure 5(p), which shows the phenomenon of swelling and blistering of the polyimide, followed by the formation of pores that gradually increase in number, size, and anisotropy, leading to the formation of anisotropic cellular networks. These 3D graphene networks become more aligned at higher fluence and eventually individual nanofibers emerge in voluminous wooly morphologies. While this model is useful in designing LINC patterns with tailored properties, further research using high speed in situ characterization methodologies is needed to reveal the temporal evolution of the LINC morphology during lasing.

Equivalence of LINC Formation on Tilted and Untilted Samples. Establishing that the LINC formation processes on the tilted and untilted samples are similar, at the same estimated fluence values, is important to generalize the results observed from the tilted experiments. The continuous nature of lasing across tilted samples could results in some dependence among the successive points along the lased path when compared with the lasing of flat untilted samples (at equivalent power, speed and z values). However, we show the equivalence between the tilted case and the untilted cases by three different approaches: analytical, numerical, and experimental.

Analytical Approach. In the first approach we show that the energetics are equivalent, which is shown in the SI (Figure S2) through average fluence calculations for both the tilted and untilted cases. However, equal fluence does not ensure similar thermal response, because fluence represents the process energetics and not the kinetics. Hence, we need to consider the time evolution of the temperature-dependent thermal diffusivity, phase transitions, and laser material interactions.

Numerical Approach. To further elucidate the equivalence of laser heating across tilted and untilted samples, we develop a 3D finite element model with temperature-dependent material properties in ANSYS APDL, in order to compare the temperatures (and rate of change of temperatures) experienced at similar levels of defocus for tilted and untilted polyimide at the same laser conditions. This technique has been used to model similar problems previously.[40,41] The beam is modeled as a Gaussian distributed heat flux at the surface of the material. Polyimide carbonization is modeled through defined temperature-dependent material properties. The details of the simulation are described in the SI (Figure S5). The used boundary conditions and problem description are shown in Figure S5, and the results are shown in Figures S6 and S7. Our simulations show that the tilted and untilted lasing at similar laser conditions can be considered equivalent from both an energetic and kinetic perspective, supporting our analytical calculations. The differences in temperature values between the flat untilted and the tilted cases are within 3% at the same levels of beam defocus (z = 0−6 mm). This result highlights the fact that equivalent fluence values lead to similar temperatures (for the same power and speed). We also observe that for the same level of beam defocus, the difference between the rate of temperature increase for the flat untilted case and the titled case is less than 20%.

Experimental Approach. In light of the results discussed above energetic and kinetic equivalence in the cases of laser heating across tilted and untilted samples, the most important aspect of equivalence is the similarity of LINC morphologies obtained in both cases. Hence, we confirm here that the LINC morphologies obtained in the case of flat untilted lasing experiments shown in Figure 5(a−i) match the morphologies resulting from tilted lasing experiments shown in Figure 2(e) at P = 18.4 W and v = 500 mm/s. This comparison between the fluence-dependent morphological transitions in both cases is plotted in Figure S8.

Fluence-Dependent Chemical Evolution. We use X-ray photoelectron spectroscopy (XPS) to characterize the fluence-dependent morphologies at several points along the lased lines (Figures 6 and S8) using the tilted sample approach shown in Figure 2 with γ = 45° at different powers. We then use the mathematical model describing the beam to correlate each point across those lines to a fluence value. Accordingly, we plot the atomic percentages of carbon, oxygen, and nitrogen as a function of fluence, as shown in Figure 6 and Tables S1−S4. Results show that carbonization increases with fluence, owing to the progressive reduction in heteroatom content (oxygen and nitrogen). A rapid drop of both oxygen and nitrogen is

https://dx.doi.org/10.1021/acsanm.1c00101
ACS Appl. Nano Mater. 2021, 4, 2973−2986

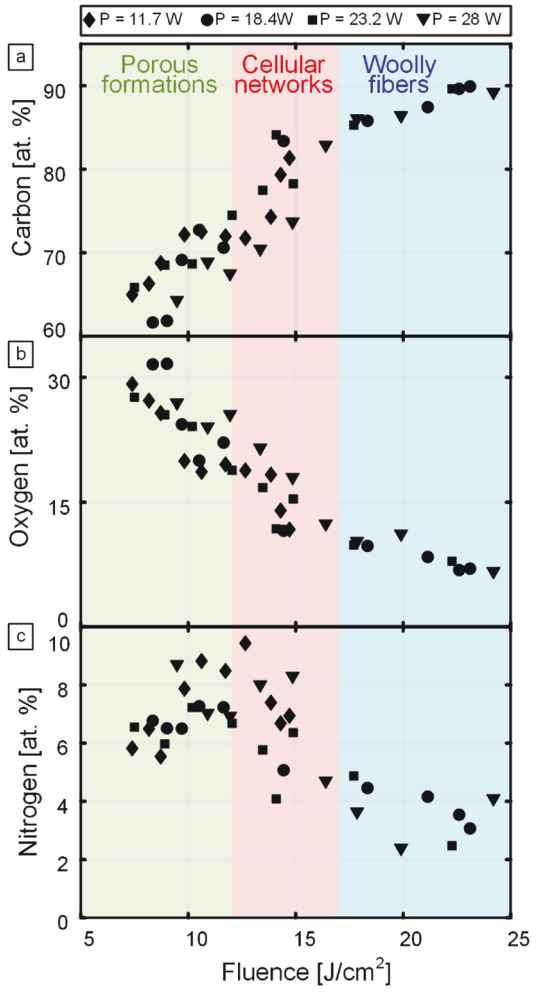

Figure 6. Fluence-dependent elemental composition of LINC from XPS measurements represented as atomic percentage for carbon in (a), oxygen in (b), and nitrogen in (c). Results plotted here are collected from 38 survey scans (Table S1−S4) at different points along the four lines lased on tilted polyimide substrate with $\gamma = 45°$ at powers of 11.7, 18.4, 23.2, and 28 W.

observed after the T1 transition, which is also clearly observed in the C 1s core scans shown in Figure S8(a), wherein the broad band between 286 and 288 eV disappear immediately after T1. This rapid loss of heteroatom content is concomitant with a marked increase in carbon content, which is also observed from the sharpening of the carbon−carbon peak in the C 1s scan (Figure S9(a)). However, after the T2 transition, slower increase in carbon and slower decrease in both oxygen and nitrogen are observed.

It is worth noting here that plotting the evolution of elemental composition as a function of fluence is more insightful than plotting these values as a function of power, because fluence is a quantity that is normalized to the spot area, which changes along the laser path in our tilted lasing experiments (i.e., we have a gradient of fluence along the lines even though the power and speed are constant, as shown in Figure 2). Also, the fact that we are lasing only individual lines with no overlapping laser paths means that the fluence values we calculate are truly representative of the energy delivered locally at each point on the substrate, as opposed to the case of rastering 2D pixel arrays (or overlapping lines), where changing power, not only changes fluence, but also increases the overlap between neighboring pixels.[1]

Insights into Coupled Physicochemical Phenomena Governing LINC Formation. Multiple processes are involved in the formation of LINC, which depend on factors like laser wavelength, laser intensity, fluence, IR absorption of the material and type of polyimide. These inputs drive the temperature and heating rate in the polyimide and hence control the level of liquification, outgassing, and carbonization that occur. This in turn affects the resulting morphology and molecular structure and hence the resulting properties. Chemical reactions also drive these processes like thermal dissociation and carbonization of the polyimide, solid−liquid phase transitions, plasma material interactions, melt expulsion, and melt dynamics driven by Marangoni convection.[42] In addition, the optical properties of the material can change, driving complex chain reactions, caused by the changing absorptivity of the material.[43] These processes can also depend on the gas environment and partial pressure. Moreover, they take place at different time scales, further complicating the phenomenon.

A number of noteworthy phenomena are observed in our experiments, which provide insight into the LINC formation process. For example, the transition to woolly fibers (T2) is clearly observed from the SEMs in Figures 4 and 5 by the drastically bigger volume of carbon, which suggests that the kinetics of forming the woolly fiber morphology is faster than the kinetics of forming cellular networks and isotropic porous morphology. Hence, the rate of outgassing during laser irradiation is higher for higher fluence, which is also supported by the XPS results indicating more loss of oxygen and nitrogen at higher fluence (Figures 6 and S9). This rapid jetting of gases out of the surface can also explain the increase of anisotropy in the porous structures that is observed after T1, as well as the alignment of the nanofibers after T2. In fact the mushroom-top geometry of LINC observed for fluence exceeding T2 (Figure 5(g−i)) resembles high speed images of laser-induced splashing of polymers from literature.[44] Such splashing dynamics of liquefied polymers could drive the formation of aligned woolly nanofibers upon rapid conversion into solid carbon. We also see evidence of melting and solidification beyond T2 in high resolution SEM images of nanofibers, in the form of spherical nanoparticles on the LINC nanofibers as shown in Figure S10, which suggest melting and beading up driven by surface energy minimization. Hence, our results indicate that the liquification and rapid solidification beyond T2 hinders graphitization of carbon and hence leads to the lower G and D peak fwhm and the disappearance of the 2D peak observed in Raman spectroscopy (Figure 4). Moreover, at even higher fluence, exceeding 25 J/cm^2, the consumption of the polyimide leads to splitting of the film as the laser either ablates, melts, and/or chemically converts the whole thickness of the film, as shown in Figure S11.

A better understanding of the chemical transformations that take place during these transitions can be built on previous pyrolysis research on the evolution and graphitization of different types of polyimide at temperatures up to 3000 °C. These studies are based on transmission electron microscopy (TEM),[45] Raman specrroscopy,[16,46] infrared spectroscopy, and outgassing observations at different temperatures. These studies show that carbonization of polyimide films occurs over two steps. Initially at a temperature of 500 °C − 650 °C there is an abrupt weight decrease of the films accompanied by

https://dx.doi.org/10.1021/acsanm.1c00101
ACS Appl. Nano Mater. 2021, 4, 2973−2986

the release of large amounts of CO and CO_2. This is followed by less weight loss and shrinkage due to evolution of small amounts of methane, hydrogen, and nitrogen which can occur over a temperature range from 800 °C to above 1000 °C.[47,48] It was also reported that nitrogen release continues in the second step of carbonization up to temperatures above 2000 °C and can be released abruptly.[49] These findings further support the hypothesis that the morphology transitions we observe (T1 and T2) are partly attributed to the rapid rate of gas released, especially when interacting with material jetting that can lead to the formation of nanofibers through rapid solidification of the jetted material. This mechanism of nanofiber formation is analogous to the fabrication of polymer nanofibers by electrospinning,[50] albeit at much higher temperatures and more rapid heating/cooling rates.

It should be noted that the in situ polyimide pyrolysis studies were carried out using relatively low heating rates (≤30 °C/min),[51] compared to rapid temperature increase rates typical in laser irradiation. Hence, they do not necessarily represent the same reaction pathways taking place during laser heating of polyimide, which is an inherently nonequilibrium process in contrast to the quasi-equilibrium process of the slow heating. Structurally, TEM studies of the pyrolyzed polyimide have shown that the slowly carbonized polyimide exhibited turbostratic structure with nanoscale elongated pores from temperatures as low as 650 °C up to temperatures as high as 2450 °C, beyond which the carbonized polyimide graphitized into high quality flat layers of graphitic carbon sheets comparable to pyrolytic carbon.[45]

Correlating LINC Morphology to Electrical Resistivity. To understand how the observed morphology transitions affects the properties of LINC, 15 mm LINC lines are lased at different z values and two power values, P = 11.7 W and P = 28.0 W in untilted configuration ($\gamma = 0°$). Using the two point probe method, the resistance divided by line length (R/L) values are calculated from multiple resistance measurements at different lengths. First, the change in spot area as a function of z, according to the beam model is plotted in Figure 7(a). The average R/L values for P = 11.7 W and P = 28 W are plotted in Figure 7(b,d), respectively. For P = 11.7 W, the polyimide is not conducting at $z > 3$ mm and $z < -3$ mm. For z between −3 and 3 mm, the average R/L values are at their highest at the edges of the range with values between 2.1 and 2.5 KΩ/mm, indicating that the connectivity of cellular networks in key for writing highly conducting LINC. These values of R/L are within the range of previously reported values for LINC.[2,21] As the spot size decreases at values around z = 0, R/L decreases to a value of around 1.65 KΩ/mm. The average carbonized line widths are noted to be ∼130 μm as illustrated from optical microscopy images in Figure S12(a).

Raman spectroscopy of these lines show a general inverse relationship between R/L values and the $I(2D)/I(G)$ ratio. Indeed, we find that LINC with a well-defined and sharp 2D peak, exhibited the lowest resistivity. The average $I(2D)/I(G)$ ratio starts at a value between 0.4−0.45, and increases for smaller spot size until a maximum value of around 0.53. Similar trends are observed in the $I(G)/I(D)$ ratio, where it reaches a maximum value of around 1.25 as shown in Figure S13. At higher power (P = 28 W), R/L values are significantly smaller (Figure 7(d)), with values ranging between 1 and 0.4 KΩ/mm when compared to the lower power case. Again a decreasing trend is observed with beam focusing, with R/L decreasing from around 1 KΩ/mm at z = 9 mm to around 0.4 KΩ/mm at

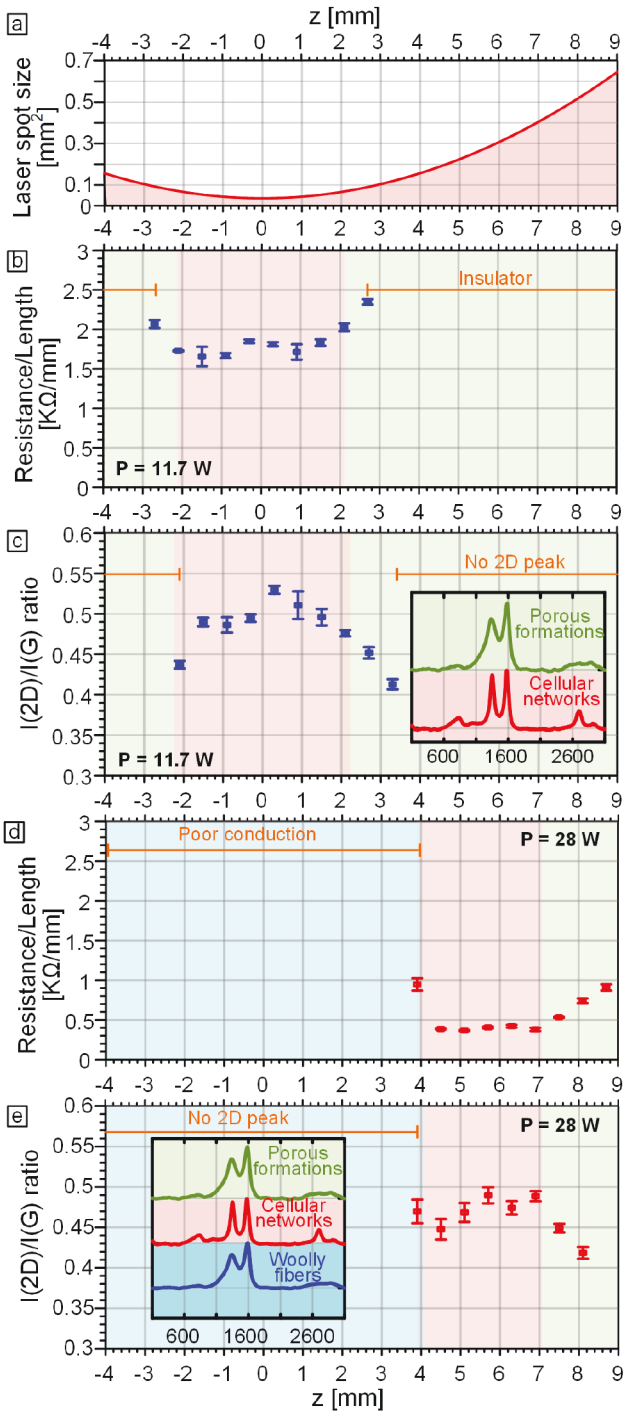

Figure 7. (a) Plot showing the change in laser spot area with z according to the laser beam profile. (b) Change in average R/L (average of 3 samples and error bars are standard deviation) with change in z value for the case of P = 11.7 W. (c) Plot representing the change in average $I(2D)/I(G)$ ratio (average of 3 samples and error bars are standard deviation) with changing spot size and fluence. (Inset in c) Raman spectra at two different morphologies. (d) Change in R/L (average of 3 samples and error bars are standard deviation) with change in z value for the case of P = 28.7 W, illustrating the drop of resistance with decreased spot size until the formations of highly insulating woolly fibers. (r) Plot representing the change in average $I(2D)/I(G)$ ratio (average of 3 samples and error bars are standard deviation) with changing spot size and fluence for P = 28.0 W. (Inset in e) Raman spectra at three different morphologies.

https://dx.doi.org/10.1021/acsanm.1c00101
ACS Appl. Nano Mater. 2021, 4, 2973−2986

z = 7 mm as the porous morphology transitions into a more anisotropic cellular networks. The average value of R/L then remains constant until the onset of the fibrous morphologies where the resistance increases drastically. At z > 4 mm (i.e., below the T2 threshold for fiber formation), the line width was measured to be ∼250 μm as shown in Figure S12(b).

The $I(2D)/I(G)$ ratio for P = 28 W are generally similar to those obtained for P = 11.7 W, with values between 0.42 at z = 8 mm, and 0.49 at z = 7 mm. Importantly, the disappearance of a sharp 2D peak at the onset of fiber formations (around z = 3.8 mm) is accompanied by a drastic drop in conductivity. The conductivity of the LINC lased at P = 28 W and v = 500 mm/s is estimated to be around 5 S/cm, matching LINC conductivities measured by other groups,[2] and superior to unannealed ink jet printed graphene.[52] The resistivity could possibly be further increased by optimizing the laser parameters such as speed or relasing.[40]

Taken together, our electrical resistivity measurements agree with the structural changes observed in our Raman spectra (Figures 3 and 4), which demonstrate that the first transition (T1) is associated with the decrease in fwhm of the G and D peaks and the emergence of the 2D peak. Relatively high fwhm in the G and D peak is typically associated with amorphous or disordered carbon and is noted in low temperature carbonization of polyimide,[16] with an expected high resistivity. However, smaller G peak fwhm is strongly correlated to the degree of graphitization and defect level,[53,54] which are crucial for lower resistivity nanocarbons. Moreover the emergence of the 2D peak is also evidence of large structural changes in the graphitic domains between T1 and T2. The $I(2D)/I(G)$ values here are similar to those previously reported in literature for laser-induced graphene,[1] confirming the presence of multilayer graphene domains.[54] Owing to the morphological transitions studied here, we expect LINC to generally be composed of different types of sp^2 carbon domains and 3D porous graphene. Disappearance of the 2D peak and increase in the fwhm of both G and D peaks are characteristics of the Raman spectra for fluence higher than the second transition (T2), producing woolly fibers with large volume.

From the resistance measurements, it is clear that these complex interactions underlying fiber formation at high fluence values result in very low conductivity LINC that is not suitable for applications as electrodes, highlighting the importance of modulating fluence during LINC formation, i.e., too small or too large fluence values prevent the formation of adequately conducting LINC. For example at v = 500 mm/s, a fluence value of F_{T2} = 17 J/cm^2 would ensure the lowest resistivity value at the selected power level. The power value can also be used to further control the line size and properties.

In order to test the mechanical robustness of LINC electrodes and the stability of their conductivity values under cyclic mechanical loading, we repeated the resistance measurement after repeated cycles of bidirectional bending. Figure S14 shows that the conductivity values remain constant even after more than 750 cycles of bending. Moreover, optical images confirm that the electrode remains strongly integrated with the flexible polyimide film with no signs of delamination or degradation, highlighting the inherent advantage of strong adhesion of LINC to polyimide.

Advantages of Fluence-Based Approach and Outlook. Two analytical approaches are typically used to understand how lasers interact with polymers. The first is the thermal approach, which focused on calculating the temperature rise in the material.[41,55,56] The second is the fluence-based approach, which focuses on calculating the delivered laser energy in the material. Thermal models require estimating material properties of polyimide and LINC and are difficult to validate experimentally since it is difficult to measure the temperature at the laser spot;[56,57] hence, they are generally more complex than fluence-based models. In this work we present a fluence-based approach for understanding LINC formation, based on Gaussian beam modeling, which is of a great utility from a manufacturing perspective.

We also focus our work on lasing individual LINC lines in air, instead of areas formed by overlapping laser paths; hence, we avoid the effect of multiple lasing of some regions on the surface, which greatly complicates the analysis and hinders extracting fundamental insights into the process-structure relationships for LINC formation. Nevertheless, we have recently shown that combining laser area rastering (that involves overlapped lines) with our fluence control approach presented here enables tailoring surface properties ranging from highly hydrophilic to highly hydrophobic.[58] Thus, our method of controlling fluence based on the degree of beam defocus can easily be extended to other applications of area rastering.

Lasing lines also have an advantage over lasing individual spots, because we can circumvent laser power transient effects that are associated with laser ramping up when starting. By ignoring the initial portion of the lased LINC lines, we ensure that steady state power is reached, when investigating the rest of the line or its end. In fact, when lasing our LINC lines it was sometimes observed that the initial spot has a drastically different morphology than the rest of the line, as shown in Figure S15, which is attributed to power transients in the laser.

In addition to elucidating the fluence-dependence of morphology, molecular structure, and electrical conductivity of LINC, our approach also enables generating maps of resulting morphologies as a function of accessible laser processing parameters, such as power and defocus, which can be easily controlled. Figure 8 shows such a morphology diagram with delineated transitions represented as iso-fluence contours, which is enabled by the insight that transitions happen at energetic threshold values of laser fluence. It is noteworthy that the morphology map shown in Figure 8 is obtained at constant lasing speed of 500 mm/s. Future investigation at different speeds will reveal the kinetic effects on the morphology, density, and properties of LINC for further tunability of electrode performance. Furnishing this fluence-based diagram is of great utility for practical purposes to facilitate replication of experimental results across different research groups using different laser processing systems. Moreover, our approach of plotting the morphology diagrams is useful for studying the influence of pressure and gas environment on LINC. Hence, more insight into the influence of these environmental factors on the evolution of both the chemistry and morphology of LINC can be obtained by carrying out fluence-dependent LINC formation studies under controlled gas conditions. In addition, our approach can also be combined with experiments wherein the molecular formulation of the polyimide precursor is engineered to modulate LINC properties.

CONCLUSIONS

Using CO_2 laser irradiation of polyimide, we demonstrated the direct formation of a variety of nanocarbons ranging from

https://dx.doi.org/10.1021/acsanm.1c00101
ACS Appl. Nano Mater. 2021, 4, 2973−2986

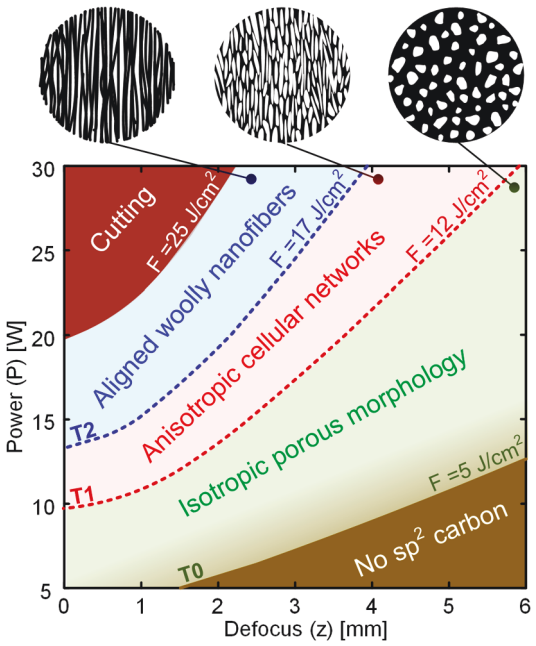

Figure 8. Morphology diagram mapping the ranges of laser parameters (power and degree of beam defocusing) for creating different types of LINC (isotropic porous morphology, anisotropic cellular networks, and aligned woolly nanofibers) for CW CO_2 laser (wavelength λ = 10.5 mm) scanning at to v = 500 mm/s. Experimentally obtained threshold fluence values for T1 and T2 are plotted as constant fluence lines (dashed).

isotropic porous carbon, highly anisotropic cellular networks of graphitic carbon, and aligned carbon nanofibers. We developed a fluence-based approach to elucidate the process-structure−property relationships governing LINC formation for these morphologies. This is achieved by mathematically modeling the effect of degree of defocus on intensity distribution and fluence for a Gaussian laser beam. We also presented an approach for creating fluence gradients on tilted polyimide films. Importantly, two specific threshold values of fluence were identified that correspond to the following: first, the transition from isotropic porous morphology to anisotropic cellular networks (T1) at a fluence value of 12 J/cm^2; second, the transition to aligned woolly nanofibers (T2) at a fluence value of 17 J/cm^2. Moreover, we show anisotropic cellular networks have the highest electrical conductivity (∼5 S/cm) for our conditions (laser wavelength of 10.6 μm and scanning speed of 500 mm/s), due to the lateral connectivity and the high graphitic content. Hence, our model and results provide insights into the physicochemical processes underlying LINC formation and enabled generating a morphology diagram of laser processing parameters.

LINC is shown to be an attractive method to fabricate porous conductive electrodes directly on flexible substrates, which are required for a wide range of applications. As an alternative to printing technologies from nanocarbon inks, LINC formation is more scalable and less costly. Taken together, our results show that material properties such as resistivity can be tuned through morphology adjustment based on local control of laser fluence. Accordingly, the variety of LINC morphologies achieved and the tunability of their properties make them superior to printing techniques that require the preparation of different nanocarbon inks for writing carbon-based electrodes with different morphologies and molecular structures on flexible substrates. Moreover the ability to control the spatial variation of morphologies and properties on the same substrate can be particularly useful in designing LINC for applications integrating high surface area nanocarbon electrodes with highly conductive and dense traces, such as for electrochemical applications.

METHODS

LINC Formation on Polyimide. Polyimide tape (TAPECASE 2B, Cat. No. 15C616), with 50 μm thickness (total thickness of 88.9 μm considering the adhesive layer) was used as a substrate precursor for LINC formation experiments. To prepare for the experiments, the tape was place on silicon wafers, and rinsed with acetone and then isopropyl alcohol for sample surface cleaning.

Direct laser irradiation on the polyimide sheets was conducted in air using a CO_2 laser cutter/engraver system (Full Spectrum Laser Pro-Series 20 × 12, 1.5 in. focus lens) with 10.6 μm wavelength and 45 W power. The system allows tuning the power by controlling the laser current. We measure the laser power at different currents using a CO_2 laser power meter (HLP-200, Changchun Laser Optoelectronics Technology Co., Ltd.). The beam radius was measured based on (1/e^2) of the maximum intensity (w_y, w_x) at different distances (z) from the beam waist using the knife-edge method.[59] The details of the approach are described in the SI. Using this technique, the beam radius at the beam waist (w_{ox}, w_{oy}), based on a Gaussian beam assumption, was determined to be 125.8 μm in the x-direction and 84 μm in the y-direction.

The laser objective lens is mounted on a motorized XY stage with a maximum speed of 500 mm/s in the X-direction. The beam spot size was controlled by adjusting the vertical distance (z) between the sample position and the beam waist; i.e., by moving the sample stage vertically with respect the objective lens. Laser power (P) was varied from 11.7 to 30.7 W, and all experiments were performed at X-direction speed (v) of 500 mm/s and under ambient conditions.

Beam Fluence Model. The beam is modeled as a nonastigmatic elliptical Gaussian beam. The beam intensity is modeled using the following relationship (as illustrated in Figure 1(a)):[60,61]

$$I(x, y, z) = I_o e^{-2\left(\left(\frac{x}{w_x(z)}\right)^2 + \left(\frac{y}{w_y(z)}\right)^2\right)}\left[\frac{W}{m^2}\right] \quad (1)$$

where x and y are measured from beam center axis at distance z from the beam waist. Beam dimensions at defocusing level (z) are w_x and w_y (as illustrated in Figure 1(d)) based on 1/e^2, and I_o is the maximum intensity.

Beam total power delivered at a spot with z vertical distance from the beam waist (estimated using thermopile measurements) is equal to the integration of the intensity over the laser spot in the horizontal plane (normal to the beam center axis), assuming complete absorption of the laser beam energy:

$$P = I_o \iint_{-\infty}^{\infty} e^{-2\left(\frac{x}{w_x}\right)^2} e^{-2\left(\frac{y}{w_y}\right)^2} dxdy \approx \frac{\pi}{2} I_o w_x w_y \quad (2)$$

where w_x and w_y are the (1/e^2) beam size.

This integration approximately gives the value of the maximum intensity:

$$I_o(z) \approx \frac{2P}{\pi w_x(z) w_y(z)} \quad (3)$$

where P is constant for different z's, however the w_x and w_y change.

The Gaussian beam size at different z values is estimated using the following equations (assuming the beam spot major and minor axis is aligned with the lasing direction x and y):

$$w_x(z) = w_{ox}\sqrt{1 + \left(\frac{M_x^2 \lambda z}{\pi w_{ox}^2}\right)^2} \quad (4)$$

https://dx.doi.org/10.1021/acsanm.1c00101
ACS Appl. Nano Mater. 2021, 4, 2973−2986

$$w_y(z) = w_{oy}\sqrt{1 + \left(\frac{M_y^2 \lambda z}{\pi w_{oy}^2}\right)^2} \quad (5)$$

where M_x^2 and M_y^2 are the beam quality factor for the x and y direction, respectively, w_{ox} and w_{oy} are the beam waist dimensions (as illustrated in Figure 1(a)). These parameters are estimated using the knife edge method as described in the SI.

The average flux I_{av} is estimated at a certain spot size for a laser power P, by averaging the intensity $I(z)$ over the spot area $A(z)$:

$$I_{av}(z) = \frac{\int_{-w_x(z)}^{w_x(z)} \int_{w_{y(z)}}^{w_y(z)} I(x, y, z)\, dy dx}{A(z)} = \frac{I_o}{\pi w_x(z) w_y(z)} \int_{-w_x(z)}^{w_x(z)} \int_{-w_y(z)}^{w_y(z)} e^{-2\left(\frac{x}{w_x(z)}\right)^2} e^{-2\left(\frac{y}{w_y(z)}\right)^2} dx dy \quad (6)$$

The average fluence F is then estimated using the following relationship:

$$F(z, v) = D(z, v) I_{av}(z) \quad (7)$$

where $D(z,v)$ is the dwell time of the laser beam over a spot. The dwell time is estimated by dividing the beam length in the lasing direction x by the beam speed v.[35]

$$D(z, v) = \frac{2w_x(z)}{v} \quad (8)$$

The average fluence of the beam on a tilted surface is shown to be approximately equal to the untilted surface average fluence for our ranges of the tilting angle γ, as discussed in the SI (Figure S2).

Characterization of LINC. SEM images of the LINC formations were taken on a Zeiss SIGMA VP Field emission scanning electron microscope. The samples were sputter coated with platinum and then imaged with a beam with an accelerating voltage of 2 kV. A XplorA Raman-AFM/TERS system microscope using 473 nm laser excitation at room temperature with a laser power of 25 mW was employed to obtain Raman spectra. XRD was conducted on a Bruker D8 Discover SRD X-ray diffractometer with Cu Kα radiation (λ = 1.54 Å). The LINC samples for XRD, were scratched from LINC lines. XPS analysis was performed using a Thermo Fisher ESCALAB 250 Xi XPS at a base pressure of 5e−9 Torr. All of the survey spectra were recorded in 1 eV step size. Elemental core spectra were recorded in 0.1 eV step sizes. All the spectra were corrected using C 1s peaks (284.5 eV) as references. The resistance of the LINC lines were measured using a Keithley two-point probe meter (model: 2100, detection limit: 100 MΩ). LINC lines of lengths 15 mm are lased in the polyimide at different z values. Each value of z and power is replicated three times. A nickel paste (PELCO Conductive Nickel Paint) was applied to the LINC lines at the measurement spots area for better contact with the probe terminals. The resistance at different lengths of LINC are measured and averaged from the three replications and used to estimate the R/L values for the LINC lines.

■ ASSOCIATED CONTENT

Supporting Information

The Supporting Information is available free of charge at https://pubs.acs.org/doi/10.1021/acsanm.1c00101.

Estimated dwell time with speed and average fluence as a function of laser power and degree of defocusing; schematic and calculations showing the effect of sample tilt on average fluence; SEMs showing the effect of laser power on woolly fiber volume; influence of the degree of defocusing on G and D peak fwhm in Raman spectra; simulation of surface temperature during lasing across flat untilted and tilted samples; core XPS scan results for C 1s, N 1s, and O 1s for LINC lines generated at different fluence values; tabulated data for atomic percentages of carbon, nitrogen, and oxygen for LINC lines generated at different fluence values; SEMs showing the formation of nanospheres during LINC formation indicating melting and beading up; SEMs showing the formation of excessive volume of woolly fibers accompanied by cutting all the way through the thickness of polyimide films at fluence higher than 25 J/cm^2; optical images of LINC lines lased at different degree of beam defocus; illustration of influence of I(G)/I(D) ratio on sample resistance; stability of LINC electrode conductivity even under 750 cycles of mechanical bending; SEMs illustrating the effect of power transients on LINC fabrication at the starting point of lased lines; and description of knife edge method (PDF) for laser beam profile characterization. (PDF)

■ AUTHOR INFORMATION

Corresponding Author

Mostafa Bedewy − *Department of Industrial Engineering, Department of Chemical and Petroleum Engineering, and Department of Mechanical Engineering and Materials Science, University of Pittsburgh, Pittsburgh, Pennsylvania 15261, United States;* orcid.org/0000-0003-4182-7533; Email: mbedewy@pitt.edu

Authors

Moataz Abdulhafez − *Department of Industrial Engineering, University of Pittsburgh, Pittsburgh, Pennsylvania 15261, United States*

Golnaz N. Tomaraei − *Department of Industrial Engineering, University of Pittsburgh, Pittsburgh, Pennsylvania 15261, United States*

Complete contact information is available at: https://pubs.acs.org/10.1021/acsanm.1c00101

Notes

The authors declare no competing financial interest.

■ ACKNOWLEDGMENTS

This research was supported by the National Science Foundation (NSF) under award number 2028580 (any opinions, findings, and conclusions or recommendations expressed in this material are those of the author(s) and do not necessarily reflect the views of the National Science Foundation). Research was also supported by Pitt Momentum Seed grant and by the Department of Industrial Engineering at the University of Pittsburgh. Characterization was performed, in part, at the Nanoscale Fabrication and Characterization Facility, a laboratory of the Gertrude E. and John M. Petersen Institute of NanoScience and Engineering, housed at the University of Pittsburgh, and in part, at Materials Characterization Laboratory, housed at Department of Chemistry in the University of Pittsburgh.

■ REFERENCES

(1) Lin, J.; Peng, Z.; Liu, Y.; Ruiz-Zepeda, F.; Ye, R.; Samuel, E. L. G.; Yacaman, M. J.; Yakobson, B. I.; Tour, J. M. Laser-Induced Porous Graphene Films from Commercial Polymers. *Nat. Commun.* **2014**, *5* (1), 5714.

(2) In, J. B.; Hsia, B.; Yoo, J.-H.; Hyun, S.; Carraro, C.; Maboudian, R.; Grigoropoulos, C. P. Facile Fabrication of Flexible All Solid-State Micro-Supercapacitor by Direct Laser Writing of Porous Carbon in Polyimide. *Carbon* **2015**, *83*, 144−151.
(3) Li, L.; Zhang, J.; Peng, Z.; Li, Y.; Gao, C.; Ji, Y.; Ye, R.; Kim, N. D.; Zhong, Q.; Yang, Y.; Fei, H.; Ruan, G.; Tour, J. M. High-Performance Pseudocapacitive Microsupercapacitors from Laser-Induced Graphene. *Adv. Mater.* **2016**, *28* (5), 838−845.
(4) Singh, S. P.; Li, Y.; Be'er, A.; Oren, Y.; Tour, J. M.; Arnusch, C. J. Laser-Induced Graphene Layers and Electrodes Prevents Microbial Fouling and Exerts Antimicrobial Action. *ACS Appl. Mater. Interfaces* **2017**, *9* (21), 18238−18247.
(5) Chen, X.; Luo, F.; Yuan, M.; Xie, D.; Shen, L.; Zheng, K.; Wang, Z.; Li, X.; Tao, L. A Dual-Functional Graphene-Based Self-Alarm Health-Monitoring E-Skin. *Adv. Funct. Mater.* **2019**, *29* (51), 1904706.
(6) Stanford, M. G.; Zhang, C.; Fowlkes, J. D.; Hoffman, A.; Ivanov, I. N.; Rack, P. D.; Tour, J. M. High-Resolution Laser-Induced Graphene. Flexible Electronics beyond the Visible Limit. *ACS Appl. Mater. Interfaces* **2020**, *12* (9), 10902−10907.
(7) Saidina, D. S.; Eawwiboonthanakit, N.; Mariatti, M.; Fontana, S.; Hérold, C. Recent Development of Graphene-Based Ink and Other Conductive Material-Based Inks for Flexible Electronics. *J. Electron. Mater.* **2019**, *48* (6), 3428−3450.
(8) Huang, Q.; Zhu, Y. Printing Conductive Nanomaterials for Flexible and Stretchable Electronics: A Review of Materials, Processes, and Applications. *Adv. Mater. Technol.* **2019**, *4* (5), 1800546.
(9) Srinivasan, R. Ablation of Polymers and Biological Tissue by Ultraviolet Lasers. *Science (Washington, DC, U. S.)* **1986**, *234* (4776), 559−565.
(10) Schumann, M.; Sauerbrey, R.; Smayling, M. C. Permanent Increase of the Electrical Conductivity of Polymers Induced by Ultraviolet Laser Radiation. *Appl. Phys. Lett.* **1991**, *58* (4), 428−430.
(11) Phillips, H. M.; Wahl, S.; Sauerbrey, R. Submicron Electrically Conducting Wires Produced in Polyimide by Ultraviolet Laser Irradiation. *Appl. Phys. Lett.* **1993**, *62* (20), 2572−2574.
(12) Feurer, T.; Sauerbrey, R.; Smayling, M. C.; Story, B. J. Ultraviolet-Laser-Induced Permanent Electrical Conductivity in Polyimide. *Appl. Phys. A: Mater. Sci. Process.* **1993**, *56* (3), 275−281.
(13) Srinivasan, R. Ablation of Polyimide (Kapton ™) Films by Pulsed (Ns) Ultraviolet and Infrared (9.17 Mm) Lasers. *Appl. Phys. A: Solids Surf.* **1993**, *56* (5), 417−423.
(14) Srinivasan, R.; Hall, R. R.; Wilson, W. D.; Loehle, W. D.; Allbee, D. C. Ultraviolet Laser Irradiation of the Polyimide, PMDA-ODA (Kapton™), to Yield a Patternable, Porous, Electrically Conducting Carbon Network. *Synth. Met.* **1994**, *66* (3), 301−307.
(15) Srinivasan, R.; Hall, R. R.; Allbee, D. C. Generation of Electrically Conducting Features in Polyimide (Kapton ™) Films with Continuous Wave, Ultraviolet Laser Radiation. *Appl. Phys. Lett.* **1993**, *63* (24), 3382−3383.
(16) Endo, M.; Hakamada, K.; Kim, C.; Miyazawa, N.; Kasai, T. Raman Spectra of Carbon Film Obtained by Pulse-Laser Irradiation to Polyimide. *Tanso* **1998**, *1998* (183), 156−161.
(17) Dyer, P. E.; Pervolaraki, M.; Lippert, T. Experimental Studies and Thermal Modelling of 1064- And 532-Nm Nd:YVO 4 Micro-Laser Ablation of Polyimide. *Appl. Phys. A: Mater. Sci. Process.* **2005**, *80* (3), 529−536.
(18) Davenas, J. Laser and Ion Beam Processing of Conductive Polyimide. *Appl. Surf. Sci.* **1989**, *36* (1−4), 539−544.
(19) Raffel, J. I.; Freidin, J. F.; Chapman, G. H. Laser-formed Connections Using Polyimide. *Appl. Phys. Lett.* **1983**, *42* (8), 705−706.
(20) Rahimi, R.; Ochoa, M.; Yu, W.; Ziaie, B. Highly Stretchable and Sensitive Unidirectional Strain Sensor via Laser Carbonization. *ACS Appl. Mater. Interfaces* **2015**, *7* (8), 4463−4470.
(21) Luo, S.; Hoang, P. T.; Liu, T. Direct Laser Writing for Creating Porous Graphitic Structures and Their Use for Flexible and Highly Sensitive Sensor and Sensor Arrays. *Carbon* **2016**, *96*, 522−531.
(22) Duan, X.; Yao, Y.; Niu, M.; Luo, J.; Wang, R.; Liu, T. Direct Laser Writing of Functional Strain Sensors in Polyimide Tubes. *ACS Appl. Polym. Mater.* **2019**, *1*, 2914−2923.
(23) Stanford, M. G.; Yang, K.; Chyan, Y.; Kittrell, C.; Tour, J. M. Laser-Induced Graphene for Flexible and Embeddable Gas Sensors. *ACS Nano* **2019**, *13*, 3474−3482.
(24) Rahimi, R.; Ochoa, M.; Ziaie, B. Direct Laser Writing of Porous-Carbon/Silver Nanocomposite for Flexible Electronics. *ACS Appl. Mater. Interfaces* **2016**, *8* (26), 16907−16913.
(25) Singh, S. P.; Ramanan, S.; Kaufman, Y.; Arnusch, C. J. Laser-Induced Graphene Biofilm Inhibition: Texture Does Matter. *ACS Appl. Nano Mater.* **2018**, *1* (4), 1713−1720.
(26) Yang, Y.; Song, Y.; Bo, X.; Min, J.; Pak, O. S.; Zhu, L.; Wang, M.; Tu, J.; Kogan, A.; Zhang, H.; Hsiai, T. K.; Li, Z.; Gao, W. A Laser-Engraved Wearable Sensor for Sensitive Detection of Uric Acid and Tyrosine in Sweat. *Nat. Biotechnol.* **2020**, *38* (2), 217−224.
(27) Tao, L.-Q.; Tian, H.; Liu, Y.; Ju, Z.-Y.; Pang, Y.; Chen, Y.-Q.; Wang, D.-Y.; Tian, X.-G.; Yan, J.-C.; Deng, N.-Q.; Yang, Y.; Ren, T.-L. An Intelligent Artificial Throat with Sound-Sensing Ability Based on Laser Induced Graphene. *Nat. Commun.* **2017**, *8* (1), 14579.
(28) Nasser, J.; Lin, J.; Zhang, L.; Sodano, H. A. Laser Induced Graphene Printing of Spatially Controlled Super-Hydrophobic/Hydrophilic Surfaces. *Carbon* **2020**, *162*, 570−578.
(29) Luong, D. X.; Yang, K.; Yoon, J.; Singh, S. P.; Wang, T.; Arnusch, C. J.; Tour, J. M. Laser-Induced Graphene Composites as Multifunctional Surfaces. *ACS Nano* **2019**, *13* (2), 2579−2586.
(30) Duy, L. X.; Peng, Z.; Li, Y.; Zhang, J.; Ji, Y.; Tour, J. M. Laser-Induced Graphene Fibers. *Carbon* **2018**, *126* (7), 472−479.
(31) Lamberti, A.; Perrucci, F.; Caprioli, M.; Serrapede, M.; Fontana, M.; Bianco, S.; Ferrero, S.; Tresso, E. New Insights on Laser-Induced Graphene Electrodes for Flexible Supercapacitors: Tunable Morphology and Physical Properties. *Nanotechnology* **2017**, *28* (17), 174002.
(32) Zeng, D. W.; Yung, K. C.; Xie, C. S. XPS Investigation of the Chemical Characteristics of Kapton Films Ablated by a Pulsed TEA CO2 Laser. *Surf. Coat. Technol.* **2002**, *153* (2−3), 210−216.
(33) Wang, R.; Duan, X.; Yao, J.; Ruan, X.; Yao, Y.; Liu, T. Processing-Structure-Property Relationship in Direct Laser Writing Carbonization of Polyimide. *J. Appl. Polym. Sci.* **2020**, *137* (34), 48978.
(34) Palm, W. J. Wavelength and Temperature Dependence of Continuous-Wave Laser Absorptance in Kapton® Thin Films. *Opt. Eng.* **2012**, *51* (12), 121802.
(35) Jiang, J.; Jacobs, A. G.; Wenning, B.; Liedel, C.; Thompson, M. O.; Ober, C. K. Ultrafast Self-Assembly of Sub-10 Nm Block Copolymer Nanostructures by Solvent-Free High-Temperature Laser Annealing. *ACS Appl. Mater. Interfaces* **2017**, *9* (37), 31317−31324.
(36) Ferrari, A. C.; Robertson, J. Raman Spectroscopy of Amorphous, Nanostructured, Diamond-like Carbon, and Nanodiamond. *Philos. Trans. R. Soc., A* **2004**, *362* (1824), 2477−2512.
(37) Koehler, T.; Frauenheim, T.; Jungnickel, G. Stability, Chemical Bonding and Vibrational Properties of Amorphous Carbon at Different Mass Density. *Phys. Rev. B: Condens. Matter Mater. Phys.* **1995**, *52* (16), 11837−11844.
(38) Drabold, D. A.; Fedders, P. A.; Stumm, P. Theory of Diamondlike Amorphous Carbon. *Phys. Rev. B: Condens. Matter Mater. Phys.* **1994**, *49* (23), 16415−16422.
(39) Piscanec, S.; Mauri, F.; Ferrari, A. C.; Lazzeri, M.; Robertson, J. Ab Initio Resonant Raman Spectra of Diamond-like Carbons. *Diamond Relat. Mater.* **2005**, *14* (3−7), 1078−1083.
(40) Biswas, R. K.; Farid, N.; O'Connor, G.; Scully, P. Improved Conductivity of Carbonized Polyimide by CO 2 Laser Graphitization. *J. Mater. Chem. C* **2020**, *8* (13), 4493−4501.
(41) Ruan, X.; Wang, R.; Luo, J.; Yao, Y.; Liu, T. Experimental and Modeling Study of CO2 Laser Writing Induced Polyimide Carbonization Process. *Mater. Des.* **2018**, *160*, 1168−1177.
(42) Otto, A.; Schmidt, M. Towards a Universal Numerical Simulation Model for Laser Material Processing. *Phys. Procedia* **2010**, *5*, 35−46.

https://dx.doi.org/10.1021/acsanm.1c00101
ACS Appl. Nano Mater. 2021, 4, 2973−2986

(43) Shin, J.; Ko, J.; Jeong, S.; Won, P.; Lee, Y.; Kim, J.; Hong, S.; Jeon, N. L.; Ko, S. H. Monolithic Digital Patterning of Polydimethylsiloxane with Successive Laser Pyrolysis. *Nat. Mater.* **2021**, *20* (1), 100−107.
(44) Fardel, R.; Urech, L.; Lippert, T.; Phipps, C.; Fitz-Gerald, J. M.; Wokaun, A. Laser Ablation of Energetic Polymer Solutions: Effect of Viscosity and Fluence on the Splashing Behavior. *Appl. Phys. A: Mater. Sci. Process.* **2009**, *94* (3), 657−665.
(45) Bourgerette, C.; Oberlin, A.; Inagaki, M. Structural and Textural Changes from Polyimide Kapton to Graphite: Part I. Optical Microscopy and Transmission Electron Microscopy. *J. Mater. Res.* **1992**, *7* (5), 1158−1173.
(46) Yoshida, A.; Kaburagi, Y.; Hishiyama, Y. Full Width at Half Maximum Intensity of the G Band in the First Order Raman Spectrum of Carbon Material as a Parameter for Graphitization. *Carbon* **2006**, *44* (11), 2333−2335.
(47) Inagaki, M.; Harada, S.; Sato, T.; Nakajima, T.; Horino, Y.; Morita, K. Carbonization of Polyimide Film "Kapton. *Carbon* **1989**, *27* (2), 253−257.
(48) Inagaki, M.; Ohta, N.; Hishiyama, Y. Aromatic Polyimides as Carbon Precursors. *Carbon* **2013**, *61*, 1−21.
(49) Hatori, H.; Yamada, Y.; Shiraishi, M. Bursting of Graphitized Polyimide Films through the Liberation of Included Nitrogen. *Carbon* **1994**, *32* (2), 359−361.
(50) Reneker, D. H.; Yarin, A. L. Electrospinning Jets and Polymer Nanofibers. *Polymer* **2008**, *49* (10), 2387−2425.
(51) Inagaki, M.; Hishiyama, Y.; Kaburagi, Y. Effect of Heating Rate during Carbonization on Graphitization of Carbon Films Derived from Aromatic Polyimides. *Carbon* **1994**, *32* (4), 637−639.
(52) Torrisi, F.; Hasan, T.; Wu, W.; Sun, Z.; Lombardo, A.; Kulmala, T. S.; Hsieh, G. W.; Jung, S.; Bonaccorso, F.; Paul, P. J.; Chu, D.; Ferrari, A. C. Inkjet-Printed Graphene Electronics. *ACS Nano* **2012**, *6* (4), 2992−3006.
(53) Katagiri, G. Raman Spectroscopy of Graphite and Carbon Materials and Its Recent Application. *Tanso* **1996**, *1996* (175), 304−313.
(54) Wu, J.-B.; Lin, M.-L.; Cong, X.; Liu, H.-N.; Tan, P.-H. Raman Spectroscopy of Graphene-Based Materials and Its Applications in Related Devices. *Chem. Soc. Rev.* **2018**, *47* (5), 1822−1873.
(55) Marla, D.; Zhang, Y.; Jabbari, M.; Sonne, M. R.; Spangenberg, J.; Hattel, J. H. A Computational Model for Heterogeneous Heating during Pulsed Laser Irradiation of Polymers Doped with Light-Absorbing Microparticles. *Appl. Phys. A: Mater. Sci. Process.* **2016**, *122* (12), 1042.
(56) Brunco, D. P.; Thompson, M. O.; Otis, C. E.; Goodwin, P. M. Temperature Measurements of Polyimide during KrF Excimer Laser Ablation. *J. Appl. Phys.* **1992**, *72* (9), 4344−4350.
(57) Dreyfus, R. W. CN Temperatures above Laser Ablated Polyimide. *Appl. Phys. A: Solids Surf.* **1992**, *55* (4), 335−339.
(58) Abdulhafez, M.; McComb, A. J.; Bedewy, M. Tailoring Surface Hydrophobicity of Commercial Polyimide by Laser-Induced Nanocarbon Texturing. *J. Micro Nano-Manufacturing* **2020**, *8* (3), 031006.
(59) Bilger, H. R.; Habib, T. Knife-Edge Scanning of an Astigmatic Gaussian Beam. *Appl. Opt.* **1985**, *24* (5), 686.
(60) Poprawe, R.; Boucke, K.; Hoffman, D. *Tailored Light 1*; Springer: New York, 2018 DOI: 10.1007/978-3-642-01234-1.
(61) Poprawe, R. *Tailored Light 2 Laser Applicaiton Technology*; Springer: New York, 2004.

https://dx.doi.org/10.1021/acsanm.1c00101
ACS Appl. Nano Mater. 2021, 4, 2973−2986